PHYSICAL REVIEW LETTERS **135,** 240801 (2025)

Editors' Suggestion

High-Fidelity Quantum State Control of a Polar Molecular Ion in a Cryogenic Environment

Dalton Chaffee,[1,2] Baruch Margulis,[1,3] April Sheffield,[1,2] Julian Schmidt,[1,2] April Reisenfeld,[1,2]
David R. Leibrandt,[4] Dietrich Leibfried,[1,2] and Chin-Wen Chou[1,2]
[1]*National Institute of Science and Technology, Boulder, Colorado 80305, USA*
[2]*Department of Physics, University of Colorado, Boulder, Colorado 80309, USA*
[3]*JILA, National Institute of Science and Technology, and University of Colorado, Boulder, Colorado, USA*
[4]*Department of Physics and Astronomy, University of California, Los Angeles, California, 90095, USA*

(Received 18 July 2025; accepted 10 November 2025; published 9 December 2025)

We use a quantum-logic spectroscopy (QLS) protocol to control the quantum state of a CaH$^+$ ion in a cryogenic environment in which reduced thermal radiation extends rotational state lifetimes by an order of magnitude over those at room temperature. By repeatedly and adaptively probing the molecule, detecting the outcome of each probe via an atomic ion, and using a Bayesian update scheme to quantify confidence in the molecular state, we demonstrate state preparation and measurement (SPAM) in a single quantum state with infidelity less than 6×10^{-3} and measure Rabi flopping between two states with greater than 99% contrast. The protocol does not require molecule-specific lasers and can be generalized, paving the way for high-fidelity quantum control of many other molecular ions.

DOI: 10.1103/7ypf-91jr

Quantum control of molecules is a burgeoning field with applications including precision measurement [1–4], quantum information processing (QIP) [5–8], and fundamental chemistry studies [9,10]. Techniques for achieving such control include direct laser cooling of molecules [11–14] and formation of molecules in a desired quantum state through association of ultracold atoms [15–17]. The fidelity of molecular state control is approaching a regime relevant for QIP applications [8,18,19], with demonstrated single-state preparation, manipulation, and measurement fidelities exceeding 90% [5,8,20,21] and those for a manifold of states above 99% [22,23]. Recently, over 99% SPAM fidelity for a single molecular hyperfine state was demonstrated for directly laser cooled neutral molecules [24]. Expanding high-fidelity quantum control capabilities to a wider variety of molecular species such as molecular ions and other applications will help to unlock molecules' full utility across quantum science.

Quantum-logic spectroscopy (QLS) in an ion trap is an established and general technique [25] that has been used to gain control over ions for which standard SPAM techniques that rely on repeatedly scattering photons are infeasible. Briefly, a "logic" ion, amenable to laser cooling and easy to control, is cotrapped with a "spectroscopy" ion that lacks an accessible cycling transition for cooling and fluorescence detection. The coupled translational motion of the two ions enables sympathetic cooling of the spectroscopy ion by the logic ion. The internal state of the spectroscopy ion can be mapped to the coupled motion and read out via the logic ion. QLS, which boasts broad applicability due to its minimal requirements on the spectroscopy ion's internal structure, has recently been applied to molecular (spectroscopy) ions with promising results in precision measurement [22,26–28] and QIP [29,30]. The practicality of molecular ions in QIP is further validated by achieving high-fidelity SPAM.

Rotational transitions in polar molecules driven by ambient thermal radiation (TR) can limit state lifetimes and SPAM fidelity in molecular quantum information experiments. For a linear molecule, rotational states are characterized by the rotational quantum number $J = 0, 1, 2, \ldots$, with energy level spacing approximately given by $h\nu_{J,J+1} \approx 2hB_R(J+1)$, where B_R is the molecule's rotational constant. TR-induced transition rates are proportional to ambient photon energy density, which for an ideal blackbody decreases superlinearly with temperature via Planck's law. Colder temperatures also reduce the number of thermally occupied rotational levels and enable lower ambient pressure, suppressing background gas collisions. Cryogenic operation is, thus, highly advantageous for controlling molecular quantum states.

In this Letter, we use QLS to control a CaH$^+$ ion in a cryogenic environment and achieve high SPAM fidelity. We observe rotational state lifetimes of $18 \pm 2(10 \pm 1)$ s for states with $J = 1(2)$, reducing the dominant error mechanism in our system by an order of magnitude over a comparable room-temperature apparatus [27,31]. Operating in a cryogenic environment dramatically reduces the size of the thermally populated molecular state space, with population found in $J \in \{1, 2, 3\}$ 97% of the time. By adaptively probing the molecule multiple times, detecting the outcome of each probe via a QLS detection protocol, and using a Bayesian probability inference scheme to quantify our confidence in the populated molecular state [32,33], we demonstrate SPAM in a single quantum state with $< 6 \times 10^{-3}$ infidelity. The detection scheme is nondestructive, and our protocol may be applied to a vast number of molecular species.

In the experiment, a $^{40}\mathrm{Ca}^+ - {}^{40}\mathrm{CaH}^+$ ion crystal [Fig. 1(a)] is trapped within a linear Paul trap [34,35]. The trap is housed inside two nested cryogenic radiation shields, with a 0.40 mT magnetic quantization field. The inner shield reaches 15.8 K under normal operating conditions (see Supplemental Material [36] for details). The Ca^+ $S_{1/2} \leftrightarrow P_{1/2}$ transition at 397 nm is used for both Doppler cooling and fluorescence detection with repumping via the $D_{3/2} \leftrightarrow P_{1/2}$ transition at 866 nm. Resolved sideband cooling of several motional modes is performed on the Ca^+ $S_{1/2} \leftrightarrow D_{5/2}$ transition at 729 nm with repumping via the $D_{5/2} \leftrightarrow P_{3/2}$ transition at 854 nm [37]. The most critical motional mode to cool is the axial, out-of-phase (OOP) mode at $\nu_m = 4.4$ MHz for mapping information from the molecule to the atom during the QLS sequence. Using a projective purification step [27], the crystal can be prepared in the motional ground state $|n = 0\rangle$ of the axial OOP mode with $> 99\%$ probability, where n is the motional quantum number.

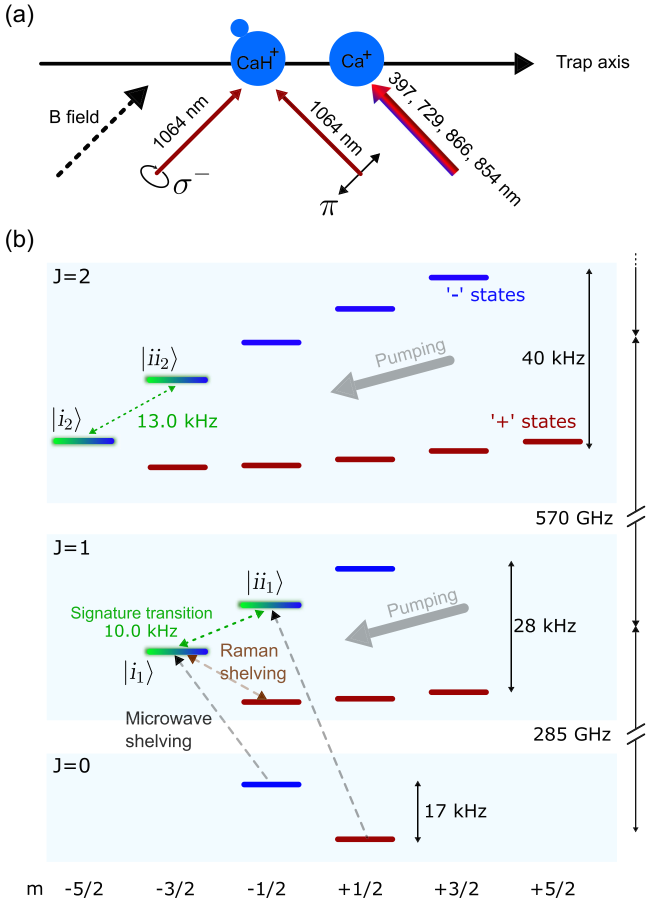

FIG. 1. (a) Schematic of the two-ion crystal, static magnetic field (quantization axis, 0.4 mT), and laser beam geometry. Molecular Raman transitions are driven by two 1064 nm beams. Doppler and sideband laser cooling of the two-ion crystal is performed on the atomic ion. (b) CaH^+ level structure. The molecule primarily occupies the $J = 0$–2 rotational manifolds and, in equilibrium, is spread over all associated spin-rotational Zeeman sublevels. While the molecular state is unknown, Raman and microwave transitions are used to pump the molecule to $|i_J\rangle$, $J \in \{1, 2, 3\}$. High-fidelity preparation (in $|i_J\rangle$) and measurement is accomplished by probing back and forth with motion-adding sidebands on the signature transition, $|i_J\rangle \leftrightarrow |ii_J\rangle$, and evaluating the result of each probe via a QLS protocol. A Raman shelving pulse that drives transitions between the prepared state ($|i_1\rangle$) and an auxiliary level ($|1, -1/2, +\rangle$) may be introduced between preparation and measurement.

In equilibrium, CaH^+ occupies a thermal mixture of rotational states within the $1\,{}^1\Sigma$ vibronic ground state. At cryogenic temperatures, rotational transitions with $\Delta J = \pm 1$ occur on an $\mathcal{O}$ (10 s) timescale, primarily due to TR, with some contribution from spontaneous decay. Each CaH^+ rotational manifold consists of $4J + 2$ sublevels spaced by $\mathcal{O}$ (10 kHz) from Zeeman splittings and spin-rotation interactions. Details of this structure and the associated pumping strategy used in this Letter have been described previously [27,31]. The molecular sublevels $|J, m, \xi\rangle$ are characterized by J, the rotational quantum number; $I = 1/2$, the spin of the hydrogen nucleus; $m = m_I + m_J$, the sum of the projection quantum numbers m_I and m_J of nuclear spin and rotational angular momentum, respectively; and ξ, which distinguishes two possible superpositions of product states $|J, m_J\rangle|I, m_I\rangle$ (with the same total m but opposite m_I) by denoting the relative sign of the superposition. For states with $m = \pm(J + I)$, ξ is defined to be the sign of m.

We identify a "signature manifold" consisting of two sublevels within each rotational manifold $J \in \{1, 2, 3\}$. We label the manifold sublevels as $|i_J\rangle \equiv |J, -J - 1/2, -\rangle$ and $|ii_J\rangle \equiv |J, -J + 1/2, -\rangle$. The "signature transition" $|i_J\rangle \leftrightarrow |ii_J\rangle$ has a unique frequency ν_J for each rotational manifold within the vibronic ground state. We drive transitions between sublevels within a rotational manifold using two Raman beams at 1064 nm with π and σ^- polarization, far detuned from any intermediate state. By setting their frequency difference to either ν_J or $\nu_J \pm \nu_m$, we address carrier or motional sideband transitions, respectively. A pumping sequence concentrates the molecular population into $|i_J\rangle$ for $J \in \{1, 2, 3\}$ when the state is unknown. Since the Raman beams can affect the nuclear spin only via coupling to molecular rotation, Raman transitions between the $J = 0$ sublevels cannot be driven. We therefore use a 285 GHz microwave drive to deshelve out of the $J = 0$ states to the $J = 1$ manifold [31]. The sublevel diagram of $J \in \{0, 1, 2\}$ and associated experimental operations are shown in Fig. 1(b).

We use a QLS protocol to determine whether the molecule occupies a particular signature manifold [27].

The sequence begins by preparing Ca^+ and the axial OOP mode in the $|D_{5/2}\rangle|n=0\rangle$ state. The Raman beams are used to probe either the $|i_J\rangle|n=0\rangle \rightarrow |ii_J\rangle|n=1\rangle$ or $|ii_J\rangle|n=0\rangle \rightarrow |i_J\rangle|n=1\rangle$ motional sideband transition. After the probe pulse, a $|D_{5/2}\rangle|n\rangle \rightarrow |S_{1/2}\rangle|n-1\rangle$ sideband pulse is applied to Ca^+, which will change the atom's electronic state only if the molecular probe has added a motional quantum to the axial OOP mode. A subsequent fluorescence detection differentiates the Ca^+ electronic states, thus determining whether a molecular transition occurred. Detection of a fluorescing Ca^+ ion ideally projects the molecule into the final state of the probed transition. CaH^+ was chosen for this Letter due to the ease of its formation via reaction of trapped Ca^+ with H_2 and the relative simplicity of its level structure from being diatomic with nuclear spin $I=1/2$. However, the QLS protocol described in this Letter may be expanded to other molecular species or for preparation in other molecular sublevels. A detailed discussion can be found in the Supplemental Material [36].

In our experiment, a single signature transition sideband probe has ∼85% population transfer efficiency. To achieve $\gtrsim 85\%$ detection fidelity, we attempt multiple nondestructive signature transition probes. Based on the binary result $R \in \{S, D\}$ (detection of Ca^+ in $|S_{1/2}\rangle$ or $|D_{5/2}\rangle$ after the QLS sequence), the confidence $P(\mathrm{in})$ that the molecule lies within the probed signature manifold is updated according to Bayes's rule [32]. Specifically, given an initial probability $P(\mathrm{in})$ that the molecule occupies the signature manifold and an outcome R of a QLS sequence, the confidence is updated according to the following:

$$P(\mathrm{in}|R) = \frac{P(R|\mathrm{in})P(\mathrm{in})}{P(R|\mathrm{in})P(\mathrm{in}) + P(R|\mathrm{out})[1-P(\mathrm{in})]}. \quad (1)$$

We empirically estimate $P(S|\mathrm{in}) = 0.85 = 1 - P(D|\mathrm{in})$, corresponding to the observed single-molecular-probe success probability after high-fidelity Bayesian state preparation, and $P(S|\mathrm{out}) = 0.009 = 1 - P(D|\mathrm{out})$, corresponding to the purification level of $|D_{5/2}\rangle|n=0\rangle$ prior to the molecular probe. A predetermined confidence threshold C_T is selected, and $P(\mathrm{in})$ is initialized to 0.5. For a detection sequence, probes are repeated until one of the following three conditions are met: $P(\mathrm{in}) > C_T$ AND the final detection with $R=S$ is on the $|ii_J\rangle|n=0\rangle \rightarrow |i_J\rangle|n=1\rangle$ transition (in-manifold detection); $1-P(\mathrm{in}) > C_T$ (out-of-manifold detection); 25 probes have been attempted.

In general, the experimental sequence is composed of "preparation," "experiment," and "measurement" stages. Preparation in $|i_J\rangle$ consists of making an in-manifold detection, possibly including pumping steps if the molecular state is initially unknown. The directionality requirement for the final probe of an in-manifold detection means that the single quantum state $|i_J\rangle$ will be prepared with high probability. Measurement consists of a detection attempt in the prepared manifold to determine whether or not the molecule still resides there. One or several experiment pulses may be applied between preparation and measurement. A detailed description of the experimental sequence, including probe logic and Bayesian probability inference, is presented in the End Matter.

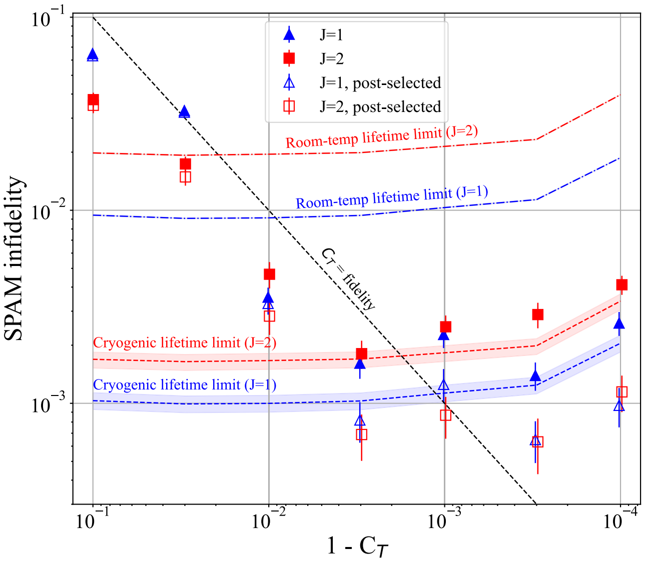

FIG. 2. Results of SPAM infidelity characterization vs confidence threshold C_T for the $J=1$ (blue triangles) and $J=2$ (red squares) signature manifolds. Infidelities are calculated by observing the fraction of measurement sequences that determine the molecule to be out of the prepared manifold immediately after preparation. Postselected infidelity omits measurements that are followed by preparation in a different rotational level. Error bars denote one Wilson interval [38]. For $C_T \lesssim 0.997$, infidelity tracks $1-C_T$ (black dashed line). Lifetime-limited infidelities are shown by blue (red) dashed curves for $J=1(2)$. Uncertainties, indicated by the shaded backgrounds, are due to uncertainties in the experimentally determined lifetimes. As C_T approaches 1, more and more probes are needed for measurement, increasing the likelihood of population loss during measurement.

To characterize SPAM fidelity within a given signature manifold, we omit the experiment stage. We define SPAM infidelity as the probability that the molecule is measured to be out of the prepared manifold after preparation. Figure 2 presents the measured SPAM infidelities for the $J=1$ and 2 signature manifolds as a function of C_T.

Varying C_T is a trade-off between confidence achieved and number of probes required per detection event. In the absence of other error mechanisms, the measured fidelity is expected to be at or above C_T (black dashed curve); this is true for our data for $C_T \leq 0.997$. For $C_T > 0.997$, other error mechanisms contribute significantly. For the C_T with the lowest infidelity, we observe an infidelity of $(1.39 \pm 0.23) \times 10^{-3}$ for $J=1$ ($C_T = 0.9997$, with an average of 2.96 probes taking 22.5 ms per measurement) and $(1.81 \pm 0.30) \times 10^{-3}$ for $J=2$ ($C_T = 0.997$, with an average of 2.37 probes taking

17.3 ms per measurement). Reported uncertainties are statistical and represent one standard deviation.

Despite the reduction in TR due to cryogenic operation, rotational level changes during measurement are the leading error mechanism at high C_T. To quantify the expected error due to rotational state change for a given data point, we compare the average duration of a measurement sequence to the observed rotational manifold lifetime. The average number of probes per measurement ranges from 2.3 to 4.9 across the range of C_T considered here, the average probe duration is 7.6 (7.3) ms for $J = 1(2)$, and the observed rotational state lifetimes are 18 ± 2 (10 ± 1) s, as detailed below. The lifetime-limited fidelities plotted in Fig. 2 are calculated by dividing the average measurement duration by the observed lifetime, representing the fraction of measurements during which a rotational state change is expected to occur. These limits provide an explanation for the increasing infidelities at high C_T (since more probes, and thus more time, are required to achieve the required confidence) and the higher infidelities for the shorter-lived $J = 2$ manifold, compared to $J = 1$, at high C_T.

To quantify contribution from other error mechanisms, we postselect away measurements that are immediately followed by preparation in a different rotational level. By doing so, we omit instances where a rotational transition has occurred during measurement. The postselected infidelity is as low as $(6.5 \pm 1.6) \times 10^{-4}$ for $J = 1$ and $(6.3 \pm 2.0) \times 10^{-4}$ for $J = 2$, both for $C_T = 0.9997$. Sources for this residual infidelity may include collisional ion reordering events and fluctuations in the signature transition sideband frequency. Further discussion is provided in the End Matter.

At 295 K, the theoretical rotational level lifetimes are about 2.0 (0.9) s for $J = 1(2)$. Both theoretical and experimentally measured [31] lifetimes are about an order of magnitude shorter than what is observed in the cryogenic environment, corresponding to an elevated theoretical fidelity limit. These limits are shown by the dot-dashed curves in Fig. 2, which are calculated according to the theoretical rotational level lifetimes and observed average measurement durations. From these limits, we infer that a room-temperature system using the same SPAM scheme would be limited to infidelities $\gtrsim 0.01$. Thus, reducing ambient TR enables improvement of SPAM infidelity by about an order of magnitude.

Since our measurement does not distinguish between states within the signature manifold, the SPAM fidelity results presented thus far cannot be considered to be of a single quantum state. Nevertheless, we expect that our preparation sequence concludes with the molecule in state $|i_J\rangle$ with near-unity probability due to the requirement that preparation ends with a $|ii_J\rangle \rightarrow |i_J\rangle$ probe. To assess the purity of the prepared state and further demonstrate our molecular quantum state control capabilities, we introduce an experimental pulse with variable duration coherently transferring population from the prepared sublevel $|i_1\rangle$ to the out-of-manifold sublevel $|1, -1/2, +\rangle$ via a Raman carrier drive. The resulting Rabi flopping, measured with C_T set to 0.997, is shown in Fig. 3. Additional data were taken near the π time for better statistics; after a π pulse, population was measured to be in manifold with $(5.6 \pm 1.2) \times 10^{-3}$ probability. We take this number as an upper bound on our single-quantum-state SPAM infidelity, though it includes some contribution from imperfect state transfer.

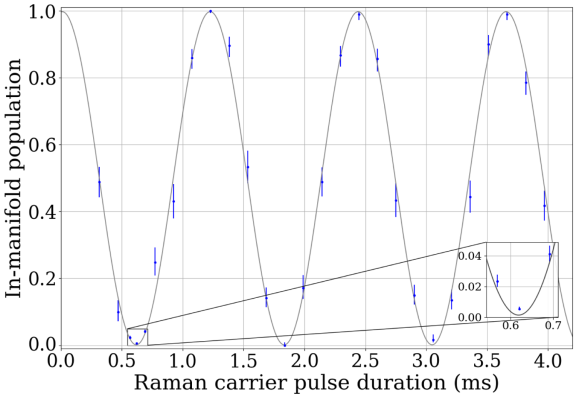

FIG. 3. Rabi flopping on $|i_1\rangle \leftrightarrow |1, -1/2, +\rangle$ by a pulse of variable duration that is resonant with the transition and applied between preparation and measurement. The fit is to an exponentially decaying sinusoidal function. After a π pulse (620 μs duration), the molecule is measured in manifold with probability $(5.6 \pm 1.2) \times 10^{-3}$. Error bars denote one Wilson interval.

By continuously attempting to prepare and measure the molecular state for $J \in \{1, 2, 3\}$, we actively track the ion's rotational state occupation and infer rotational level lifetimes. Doing so, we can extract information about the TR environment interacting with the ion, assuming rotational transitions are driven solely by TR [31]. The population

TABLE I. Rotational level tracking. The lifetime is found by dividing the total time spent within a level by the number of times the molecule was observed to leave the state. The effective BBR temperature is found by comparing the observed lifetime to theory [31,39]. Uncertainties in measured lifetimes are statistical, while uncertainties in inferred BBR temperatures include both statistical contributions and uncertainty in the molecule's permanent dipole moment [40]. We cannot directly measure population in $J = 0$, but we assume the molecule has transitioned there if it is detected in $J = 1$ only after a $J = 0 \rightarrow 1$ deshelving pulse. The unaccounted-for 0.03 population fraction is attributed primarily to occupation of $J > 3$, which we do not attempt to detect.

J	Occupation fraction	Lifetime (s)	BBR temperature (K)
1	0.48	18.1 ± 1.8	$42.0^{+4.3}_{-3.7}$
2	0.36	10.2 ± 0.9	$33.6^{+3.2}_{-2.9}$
3	0.13	5.5 ± 0.6	$30.6^{+4.1}_{-3.6}$

fractions, ion lifetimes, and inferred blackbody temperature for each rotational state $J \in \{1, 2, 3\}$ are shown in Table I. These data were obtained by tracking the molecular rotational level for about 1 hour by running SPAM experiments with C_T set to 0.997. Note that the ion was actively deshelved out of $J = 0$ if suspected to reside there. The blackbody radiation (BBR) temperature is inferred from the lifetime assuming an ideal blackbody environment.

The inferred photon densities are significantly higher than what would be expected from thermal equilibrium with the measured inner shield temperature of 15.8 K. Moreover, considering the occupation fractions of the various J levels, we find that the distribution is most consistent with a BBR temperature of 34 K [41]. We have ruled out elevated trap RF electrode temperature, TR leakage, and background gas collisions as possible explanations for this observation. Additional hypotheses include laser beams-induced effects and geometrical effects. Further discussion can be found in the Supplemental Material [36]. Identification and characterization of the leading mechanism causing the observed discrepancy is beyond the scope of this Letter.

In summary, we have demonstrated high-fidelity molecular quantum state control, achieving better than 99.8% SPAM fidelity within signature manifolds and above 99.4% quantum state transfer, setting a lower bound on our single-state SPAM fidelity. We also measure enhanced rotational state lifetimes due to reduced thermal radiation. The versatile QLS protocol in a cold thermal environment constitutes a pristine setting for studying numerous molecular ion species. While CaH^+ was chosen as a proof of principle, its sublevels can serve as decent qubits with low sensitivity (on the order of 10 kHz/mT) to magnetic field fluctuations and experimentally determined state lifetimes of longer than 10 s in a cryogenic environment. Nonpolar molecular ions promise to have much longer state lifetimes and to be even better qubits, provided they can be adequately prepared and controlled with quantum logic. The high-fidelity quantum state control and generalizability of our apparatus promises to enable a new regime of precision measurement, QIP, and chemistry applications with molecules.

Acknowledgments—We thank D. B. Hume and A. Kwiatkowski for their careful reading of the manuscript. This work is supported by the Army Research Office, Agreement No. 22X027, and the Air Force Office of Scientific Research, Grant No. FA9550-23-1-0028. B. M. acknowledges the support of the Rothschild Foundation. J. S. was supported by the Alexander von Humboldt Foundation.

Data availability—The data that support the findings of this article are available from the authors upon reasonable request.

[1] W. B. Cairncross, D. N. Gresh, M. Grau, K. C. Cossel, T. S. Roussy, T. Ni, Y. Zhou, J. Ye, and E. A. Cornell, Phys. Rev. Lett. **119**, 153001 (2017).

[2] O. Grasdijk, O. Timgren, J. Kastelic, T. Wright, S. Lamoreaux, D. DeMille, K. Wenz, M. Aitken, T. Zelevinsky, T. Winick, and D. Kawall, Quantum Sci. Technol. **6**, 044007 (2017).

[3] J. J. Hudson, D. M. Kara, I. Smallman, B. E. Sauer, M. R. Tarbutt, and E. A. Hinds, Nature (London) **473**, 493 (2011).

[4] J. Baron, W. Campbell, D. DeMille, J. Doyle, G. Gabrielse, Y. Gurevich, P. Hess, N. Hutzler, E. Kirilov *et al.* (ACME Collaboration), Science **343**, 269 (2014).

[5] Y. Bao, S. S. Yu, L. Anderegg, E. Cahe, W. Ketterle, K.-K. Ni, and J. Doyle, Science **382**, 1138 (2023).

[6] C. M. Holland, Y. Lu, and L. W. Cheuk, Science **382**, 1143 (2023).

[7] V. V. Albert, J. P. Covey, and J. Preskill, Phys. Rev. X **10**, 031050 (2020).

[8] L. R. B. Picard, A. J. Park, G. E. Patenotte, S. Gebretsadkan, D. Wellnitz, A. M. Rey, and K.-K. Ni, Nature (London) **637**, 821 (2024).

[9] H. Son, J. J. Park, Y.-K. Lu, A. O. Jamison, T. Karman, and W. Ketterle, Science **375**, 1006 (2022).

[10] O. A. Krohn, K. J. Catani, J. Greenberg, S. P. Sundar, G. da Silva, and H. J. Lewandowski, J. Chem. Phys. **154**, 074305 (2021).

[11] E. S. Shuman, J. F. Barry, and D. DeMille, Nature (London) **467**, 820 (2010).

[12] D. Mitra, N. B. Vilas, C. Halla, L. Anderegg, B. L. Augebraum, L. Baum, C. Miller, S. Raval, and J. M. Doyle, Science **369**, 1366 (2020).

[13] G.-Z. Zhu, D. Mitra, B. L. Augenbraun, C. E. Dickerson, M. J. Frim, G. Lao, Z. D. Lasner, A. N. Alexandrova, W. C. Campbell, J. R. Caram *et al.*, Nat. Chem. **14**, 995 (2022).

[14] S. Truppe, H. Williams, M. Hambach, L. Caldwell, N. Fitch, E. Hinds, B. Sauer, and M. Tarbutt, Nat. Phys. **13**, 1173 (2017).

[15] W. B. Cairncross, J. T. Zhang, L. R. B. Picard, Y. Yu, K. Wang, and K.-K. Ni, Phys. Rev. Lett. **126**, 123402 (2021).

[16] D. K. Ruttley, A. Guttridge, S. Spence, R. C. Bird, C. R. L. Sueer, J. M. Hutson, and S. L. Cornish, Phys. Rev. Lett. **130**, 223401 (2023).

[17] C. He, X. Nie, V. Avalos, S. Botsi, S. Kumar, A. Yang, and K. Dieckmann, Phys. Rev. Lett. **132**, 243401 (2024).

[18] V. V. Albert, J. P. Covey, and J. Preskill, Phys. Rev. X **10**, 031050 (2020).

[19] K.-K. Ni, T. Rosenband, and D. D. Grimes, Chem. Sci. **9**, 6830 (2018).

[20] L. Christakis, J. S. Rosenberg, R. Raj, S. Chi, A. Morningstar, D. A. Huse, Z. Z. Yan, and W. S. Bakr, Nature (London) **614**, 64 (2023).

[21] D. K. Ruttley, A. Guttridge, T. R. Hepworth, and S. L. Cornish, PRX Quantum **5**, 020333 (2024).

[22] M. Sinhal, Z. Meir, K. Najafian, G. Hegi, and S. Willitsch, Science **367**, 6483 (2020).

[23] M. Roguski, A. Shlykov, Z. Meir, and S. Willitsch, arXiv:2504.02642.

[24] C. M. Holland, Y. Lu, S. J. Li, C. L. Welsh, and L. W. Cheuk, Phys. Rev. X **15**, 031018 (2025).

[25] P. O. Schmidt, T. Rosenband, C. Langer, W. M. Itano, J. C. Bergquist, and D. J. Wineland, Science **309**, 749 (2005).

[26] F. Wolf, Y. Wan, J. C. Heip, F. Gerbert, C. Shi, and P. O. Schmidt, Nature (London) **530**, 457 (2016).

[27] C. W. Chou, C. Kurz, D. B. Hume, P. N. Plesso, D. R. Leibrandt, and D. Leibfried, Nature (London) **545**, 203 (2017).

[28] D. Holzapfel, F. Schmid, N. Schwegler, O. Stadler, M. Stadler, A. Ferk, J. P. Home, and D. Kienzler, Phys. Rev. X **15**, 031009 (2025).

[29] Y. Lin, D. R. Leibrandt, D. Leibfried, and C.-W. Chou, Nature (London) **581**, 273 (2020).

[30] L. Qi, E. C. Reed, B. Yu, and K. R. Brown, arXiv:2411.07137.

[31] Y. Liu, J. Schmidt, Z. Liu, D. R. Leibrandt, D. Leibfried, and C.-W. Chou, Science **385**, 790 (2024).

[32] D. Hume, T. Rosenband, and D. J. Wineland, Phys. Rev. Lett. **99**, 120502 (2007).

[33] S. D. Erickson, J. J. Wu, P.-Y. Hou, D. C. Cole, S. Geller, A. Kwiatkowski, S. Glancy, E. Knill, D. H. Slichter, A. C. Wilson *et al.*, Phys. Rev. Lett. **128**, 160503 (2022).

[34] D. J. Wineland, C. Monroe, W. M. Itano, D. Leibfried, B. E. King, and D. M. Meekhof, J. Res. Natl. Inst. Stand. Technol. **103**, 259 (1998).

[35] S. M. Brewer, J.-S. Chen, A. M. Hankin, E. R. Clements, C.-W. Chou, D. J. Wineland, D. B. Hume, and D. R. Leibrandt, Phys. Rev. Lett. **123**, 033201 (2019).

[36] See Supplemental Material at http://link.aps.org/supplemental/10.1103/7ypf-91jr for more details about the apparatus, discussion of the possibilities of extending the methods to other molecular states and species, and additional measurements towards determining the limiting factor(s) of the observed molecular state lifetimes.

[37] C. Roos, T. Zeiger, H. Rohde, H. C. Nägerl, J. Eschner, D. Leibfried, F. Schmidt-Kaler, and R. Blatt, Phys. Rev. Lett. **83**, 4713 (1999).

[38] E. B. Wilson, J. Am. Stat. Assoc. **22**, 209 (1927).

[39] J. Koelemeij, B. Roth, and S. Schiller, Phys. Rev. A **76**, 023413 (2007).

[40] A. L. Collopy, J. Schmidt, D. Leibfried, D. R. Leibrandt, and C.-W. Chou, Phys. Rev. Lett. **130**, 223201 (2023).

[41] S. Patel and K. R. Brown, J. Phys. Chem. A **129**, 3624 (2025).

End Matter

Bayesian detection sequence—A flowchart representing the experimental sequence, including the preparation, experiment, and measurement stages, is presented in Fig. 4. Preparation may involve many pumping pulses if the initial state is unknown. The "pump within J to $|i_J\rangle$" action consists of multiple rounds of cooling to the motional ground state and then driving directional, motion-adding sidebands on molecular transitions to move the molecular population from any initial sublevel to $|i_J\rangle$. To detect the molecule when it is initially in the $J=0$ manifold, we deshelve the population from $J=0$ into $|i_1\rangle$ by executing $|J=0,m=-1/2,\xi=-\rangle \leftrightarrow |i_1\rangle$ and $|J=0,m=1/2,\xi=+\rangle \leftrightarrow |ii_1\rangle$ deshelving pulses using a 285 GHz microwave source. A subsequent successful preparation in $J=1$ indicates that the molecule was originally in $J=0$ but prepared in $|i_1\rangle$.

"Partial pump" refers to a pumping pulse on the $|ii_J\rangle \rightarrow |i_J\rangle$ transition (and in $J=1$, a preceding $|iii_1\rangle \equiv |J=1,m=+1/2,\xi=-\rangle \rightarrow |ii_1\rangle$ pumping pulse). This action is necessary due to a small probability to transfer the molecular state without an $|S\rangle$ detection (as well as the possibility of off-resonant excitation from $|ii_1\rangle \rightarrow |iii_1\rangle$). Because of partial pumping, the Bayesian detection sequence does not strictly detect one particular initial sublevel, but rather, either sublevel in the signature manifold (and for $J=1$, including $|iii_1\rangle$).

The recorded result of a measurement typically corresponds to the result ("in manifold" or "out of manifold") of its Bayesian state detection sequence. However, in the rare case where the detection sequence terminates due to hitting the maximum allowed number of probes (and thus, with $1-C_T < \mathrm{P(in)} < C_T$) we assign an in-manifold result for $\mathrm{P(in)} > 0.5$ and out-of-manifold result for $\mathrm{P(in)} < 0.5$.

At the conclusion of state preparation, we would like to ensure that the molecule resides in one particular sublevel ($|i_J\rangle$ for the experiments presented here). To do that, we require that $|m_g\rangle = |i_J\rangle$ before completing an in-manifold detection. This requirement has the added benefit that preparation can be bypassed after an in-manifold measurement, as indicated in the Experimental Sequence panel of Fig. 4.

Error budget—By postprocessing our data, we extract information about various error mechanisms affecting our signature manifold SPAM fidelity. Errors due to TR-induced loss are inferred by counting the number of instances in which an out-of-manifold measurement was followed by preparation in a different J manifold (i.e., taking the difference between the raw and postselected infidelities plotted in Fig. 2). Another possible error mechanism is changes in ion order due to collisions with background gas, which will cause a decrease in detection fidelity due to the change in light shift magnitude for the molecular levels induced by the tightly focused Raman beams. During SPAM experiments, the ion order is checked and reset as necessary every 15 measurements. We can estimate the infidelity contribution by calculating the fidelity increase when postselecting away all sets of 15 measurements that are followed by detection of an ion reorder; from this, we infer a contribution of $< 2.6 \times 10^{-4}$ for all experimental

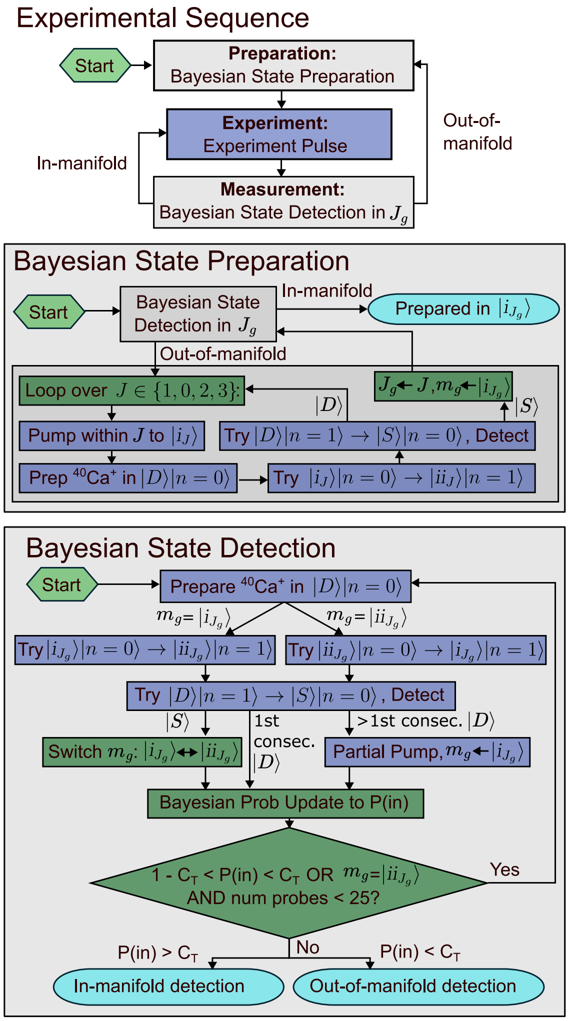

FIG. 4. Full experimental sequence including Bayesian state preparation and detection. Here, J_g and $|m_g\rangle$ are the system's current determined molecular rotational and signature manifold state, respectively: they are initialized to $J_g = 1$ and $|m_g\rangle = |i_J\rangle$. Gray boxes represent subprotocols expanded elsewhere in the flowchart, dark blue boxes indicate physical actions performed on the ions, green boxes indicate software logic updates, and light blue ovals indicate the endpoint of a subprotocol. The experimental sequence is performed (with occasional breaks for ion order check and servo experiments) until the desired amount of data has been collected.

conditions presented. This is consistent with our observed reorder rate (~1 reorder/3 minutes from an independent measurement) and the decrease in detection fidelity we observe when purposefully operating in the "wrong" ion order.

Another error mechanism arises from the subunity confidence threshold. This error occurs when a sufficiently large number of false-negative outcomes leads to an inaccurate out-of-manifold detection. Assuming the false negative and false positive probabilities used in the Bayesian update are accurate, this error will always be $\leq 1 - C_T$. To quantify more precisely, we estimate subunity C_T error as the average confidence $P(\text{in})$ obtained at the conclusion of Bayesian state detection for out-of-manifold measurements. If this estimate exceeds the postselected infidelity including ion reorder, the contribution from subunity C_T is instead taken to be the postselected infidelity. Otherwise, the remaining discrepancy reflects residual error due to mechanisms beyond TR-induced loss, subunity C_T, or ion reorder. We attribute these remaining errors ("other mechanisms") chiefly to signature transition frequency fluctuations, which can increase the actual false

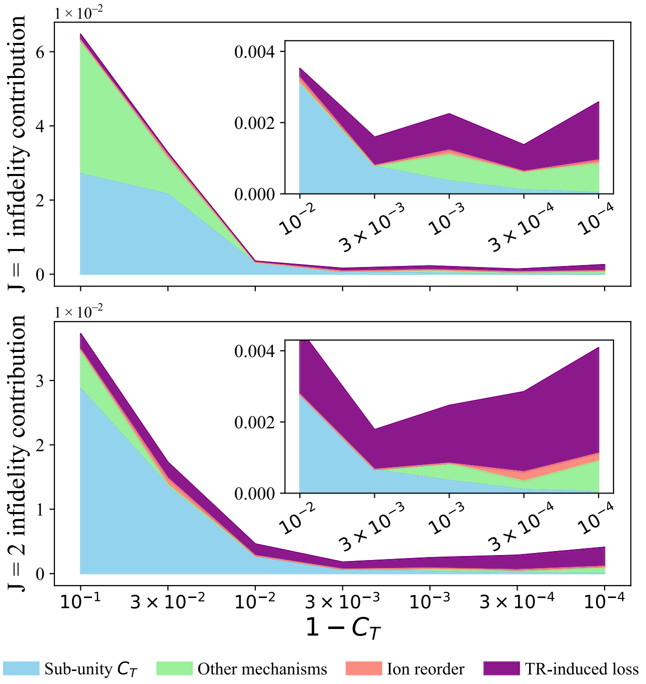

FIG. 5. Comparison of infidelity mechanism contributions vs C_T. At low C_T, most errors are attributable to the subunity threshold, while at high C_T, TR-induced loss dominates.

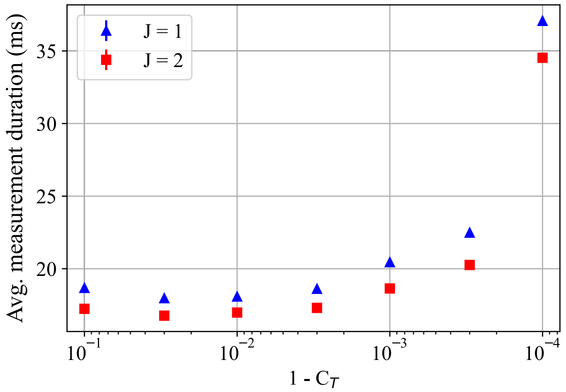

FIG. 6. Average measurement duration vs C_T. As C_T increases above 0.97, more probes are required to cross threshold, increasing the average measurement duration. Statistical error bars are smaller than the plotted markers.

negative probability $P(D|\mathrm{in})$. In this case, $P(\mathrm{in})$ will not be faithfully estimated by application of Eq. (1). Though we interleave servos of several parameters whose drifts can cause shifts in the signature transition sideband frequency—such as axial OOP motional mode frequency, Raman beam intensities, and micromotion—some drift still occurs. Such errors could be mitigated by more frequent calibration of the signature transition sideband pulse parameters and technical improvements to reduce drifts.

The results of this analysis are displayed in Fig. 5. As expected, contribution from subunity C_T falls off with increasing C_T. Meanwhile, the TR-induced loss errors increase with increasing C_T due to the increased average measurement duration. A plot of the average measurement duration for each experiment condition is shown in Fig. 6.